


## Article

# Application of CFD Modelling for Pollutant Dispersion at an Urban Traffic Hotspot

Giannis Ioannidis <sup>1</sup>, Chaofan Li <sup>2</sup>, Paul Tremper <sup>2</sup>, Till Riedel <sup>2</sup> and Leonidas Ntziachristos <sup>1,\*</sup> 

<sup>1</sup> Mechanical Engineering Department, Aristotle University of Thessaloniki, GR 54124 Thessaloniki, Greece; giannisi@auth.gr

<sup>2</sup> Karlsruhe Institute of Technology (KIT), TECO/Pervasive Computing Systems, 76131 Karlsruhe, Germany; chaofan.li@kit.edu (C.L.); paul.tremper@kit.edu (P.T.); riedel@teco.edu (T.R.)

\* Correspondence: leon@auth.gr

**Abstract:** Health factors concerning the well-being of the urban population urge us to better comprehend the impact of emissions in urban environments on the micro-scale. There is great necessity to depict and monitor pollutant concentrations with high precision in cities, by constructing an accurate and validated digital air quality network. This work concerns the development and application of a CFD model for the dispersion of particulate matter, CO, and NO<sub>x</sub> from traffic activity in a highly busy area of the city of Augsburg, Germany. Emissions were calculated based on traffic activity during September of 2018 with COPERT Street software version 2.4. The needed meteorological data for the simulations were taken from a sensor's network and the resulting concentrations were compared and validated with high-precision air quality station indications. The model's solver used the steady-state RANS approach to resolve the velocity field and the convection–diffusion equation to simulate the pollutant's dispersion, each one modelled with different molecular diffusion coefficients. A sensitivity analysis was performed to decide the most efficient computational mesh to be used in the modelling. A velocity profile for the atmospheric boundary layer (ABL) was implemented into the inlet boundary of each simulation. The cases concerned applications on the street level in steady-state conditions for one hour. The results were evaluated based on CFD validation metrics for urban applications. This approach provides a comprehensive state-of-the-art 3D digital pollution network for the area, capable of assessing contamination levels at the street scale, providing information for pollution reduction techniques in urban areas, and combining with existing sensor networks for a more thorough portrait of air quality.

**Keywords:** CFD; OpenFOAM; pollutant dispersion; traffic emissions; urban environment; NO<sub>x</sub>; CO; PM



**Citation:** Ioannidis, G.; Li, C.; Tremper, P.; Riedel, T.; Ntziachristos, L. Application of CFD Modelling for Pollutant Dispersion at an Urban Traffic Hotspot. *Atmosphere* **2024**, *15*, 113. <https://doi.org/10.3390/atmos15010113>

Academic Editor: Patrick Armand

Received: 22 November 2023

Revised: 4 January 2024

Accepted: 15 January 2024

Published: 18 January 2024



**Copyright:** © 2024 by the authors. Licensee MDPI, Basel, Switzerland. This article is an open access article distributed under the terms and conditions of the Creative Commons Attribution (CC BY) license (<https://creativecommons.org/licenses/by/4.0/>).

## 1. Introduction

Urban air quality is one of the most important aspects of human well-being. Poor atmospheric conditions are connected to health issues, respiratory diseases [1], and psychological implications [2]. It is, therefore, necessary to understand and accurately predict the behavior of toxic compounds within small scale layers to estimate the impact these pollutants have on human life.

Traffic activity is a major source of air pollution within the urban atmospheric layer. Reşitoglu et al. (2015) [3] pointed out that 40–70% of NO<sub>x</sub> detected in urban areas originates from traffic. Li et al. (2018) [4] performed source apportionment analysis on ultrafine particles concentrated in an urban environment and concluded that 41% came from vehicle exhaust. Angatha and Mehar (2020) [5] mentioned that road transport contributes about 50–80% of the CO concentrations in developing countries. NO<sub>x</sub> emissions are responsible for ozone and smog formation in large metropolitan areas [6]. Fine particulate matter infiltrates the lungs and can cause respiratory issues and problems [4]. Carbon monoxide

is primarily produced by incomplete combustion, and it is connected to cardiovascular diseases [7]. Thus, it is essential to investigate the formation, dispersion, and concentration of these compounds in highly populated areas where the urban population is exposed. To achieve this, air quality models are used to accurately predict the distribution of pollutants according to the corresponding meteorological conditions, emission rates, and geometrical configurations.

Understanding the dynamics of air flow is crucial in correctly depicting pollutant distribution within the urban landscape. Capturing turbulent flow phenomena and modelling gas dispersion within idealized street canyons has been the target of several literature studies. Such applications have mainly focused on studying geometrical layouts that resemble urban environments, to examine different parameters that affect pollutant dispersion using CFD models. Yazid et al. (2014) [8] demonstrated the impact that different geometrical shapes have on passive pollutant dispersion. They concluded that buildings with sharp roofs enhance the recirculation of the pollutant. Tee et al. (2020) [9] examined the dependence of normalized gas concentrations on the turbulent Schmidt number ( $Sc_t$ ) between two idealized buildings and found this was an important parameter for modelling accuracy. Montazeri and Blocken (2013) [10] performed an analysis of the impact that buildings with and without balconies have on wind-induced pressure coefficients. They observed that the presence of balconies can change by up to two-fold the wind pressure distribution along the buildings. Su et al. (2019) [11] studied the influence of tree planting on a street scale and found up to 27% increased concentrations, compared to the no-trees case. Fernández-Pacheco et al. (2023) [12] used CFD modelling to examine the dispersion of  $PM_{10}$  in a large-scale area, containing the city of Gijón, Spain. They validated the numerical findings by applying the same wind conditions on a wind tunnel replica of the area with satisfactory accuracy. Although these studies extensively examined different parameters affecting pollutant dispersion, they either only refer to an idealized environment and they did not use meteorological or emission data, or the scale of the application did not allow for street scale pollution identification.

A number of detailed data are required to model pollutant dispersion in a real urban environment. Street and buildings geometry, emission rates, and meteorological data are prerequisites for examining the dispersion of pollutants in real urban scenarios. Numerous methods can be used for urban micro-scale modelling including Lagrangian and Eulerian models. Toscano et al. (2021) [13] performed a comparison of the performance of ship plume modelling against observations in the city of Naples between a Gaussian dispersion model (CALPUFF) and a CFD model. They found that for air quality stations positioned in street canyons, where turbulence effects are enhanced, the CFD model provides better results compared to CALPUFF that showed consistent underestimation. The SCIPPER project examined the contribution of ship emissions in the city of Marseille by applying Lagrangian (PMSS) and CFD (ANSYS) methods. It was found that the CFD model accurately depicts wind behavior in high turbulence areas and that it computes pollutant concentration levels that deviate 23% compared to 34% with PMSS against measurements [14]. CFD modelling is considered to produce adequate wind flows in complex geometrical configurations such as cities, compared to other models, and this is the reason why it was selected for this work. There are a few attempts in previous literature studies to simulate pollutants dispersion from traffic using CFD within real-world urban conditions. Lauriks et al. (2021) [15] examined the contribution of traffic-related  $NO_2$  and  $PM_{10}$  to urban air pollution in a main road artery of Antwerp. A limitation of the work was that it only considered a single wind direction. Sanchez et al. (2017) [16] used the Reynolds-Average Navier–Stokes (RANS) approach to simulate  $NO_x$  dispersion in a traffic hotspot in Madrid under different traffic emission scenarios. No other pollutants were considered. Rivas et al. (2019) [17] studied the dispersion of traffic  $NO$  and  $NO_2$  in the entire city of Pamplona also using RANS and established a regression coefficient of 0.68 with hourly measured values. Again, no other pollutant was considered in this study. Akhatova et al. (2015) [18] examined the dispersion of exhaust  $CO$  in a traffic-loaded street of Astana using seasonal wind direction and speed,

and traffic emission averages. This approach referred to seasonal averages and did not distinguish daily traffic trends, and again only concerned one traffic-related pollutant.

There is great need to accurately depict air pollution in urban environments for as many contaminants as possible to have a complete and clear view of pollution levels in cities. Until now, no work has been found in the literature that uses a CFD approach to directly simulate CO, particulate matter, and NO<sub>x</sub> from vehicular activity in a city. This could be attributed to a lack of emission data. For this reason, this work focuses on modelling the dispersion of pollutants from road traffic, mainly NO<sub>x</sub>, CO, and PM in a highly trafficked activity area. The work demonstrated in this paper also focuses on providing high spatial resolution of concentrations, showing variability of pollution levels in constrained areas, in the time scales examined. So, a realistic and validated CFD model such as this provides a clear portrait of concentration levels at the corresponding urban area, with focus on street scale. It builds a three-dimensional gradient of the contaminants with high spatial resolution so that the information could be used as a guide for various applications. Urban planners can use this model as a guide to recognize areas of high pollutant concentrations during a selected period and to examine different building configurations for the minimization of pollution at the street scale. The modelled outputs could also provide the necessary information to calibrate and verify existing low-cost air quality networks that are not enough to give a full-lengthed picture of air pollution in the frameworks of smart cities applications. This is why the work presented in this paper shares an important role in assessing air quality and minimizing pollution in urban areas, with a focus on areas not containing observed indications and where direct exposure from traffic activity can be acknowledged.

## 2. Methodology

### 2.1. Area of Interest and Geometrical Model

The area selected for the simulations was a  $650 \times 1050 \text{ m}^2$  area that is situated at the northern boundary of the city center of Augsburg. It consists of buildings with an average height of 18 m with the tallest structure being a chapel that stands at 56 m. In the middle of the study area, in Karlstraße street, at (10.896, 48.370) and at a height of 2.5 m from the ground, there is an air quality station operated by the Bavarian State Office for the Environment (LfU). In Figure 1b, it is shown that on the northern side of the city there is also an urban background station at Bourges-Platz and that on the southern side of the city, and LfU background station is used to measure regional background concentrations. Both background stations are also operated by the Bavarian State Office for the Environment. The devices records concentrations of NO, NO<sub>2</sub>, CO, PM<sub>10</sub>, and O<sub>3</sub> in  $\mu\text{g}/\text{m}^3$  with an hourly temporal resolution. The main road artery that represents most of the traffic activity starts from Prinzregentenstraße street (Figure 2a (A)) and ends at Pilgerhausstraße street (Figure 2a (B)).

The 3D model of the city was acquired from Open Street Maps (OSM). To simulate the dispersion of the pollutants from traffic activity, emission sources were placed in the model along the main arterial road, to include the area containing the air quality station. These sources were rectangle-shaped elements in the computational domain representing sections of the route on which vehicles are driven on, with a width of 8 m, the same as the width of the road. Figure 2b shows the top view of the digital geometrical model and it shows that seven different emission sources were placed from point A to point B. For designing the computational domain, Blocken (2015) [19] suggested a minimum height of 6 H and an upstream distance of 5 H, with H being the height of the tallest building. Zheng et al. (2021) [20] recommended a domain height of 7.5 H and an upstream distance also of 5 H for street canyons modelling using LES. Tominaga et al. (2008) [21] suggested a domain height of 6 H with H being the height of the target building. Pantusheva et al. (2022) [22], when reviewing common practices followed on CFD applications, found that a minimum 6 H height was used in 57% of the cases and an upstream distance of at least 5 H in 46% of the cases. Therefore, for this work, a domain height of 350 m was used



(>6 H) and the distance between the boundaries and the closest building on each side was 300 m (>5 H), creating a domain of  $1250 \times 1650 \text{ m}^2$  in size. In Figure 2b, the created computational domain shows the dimensions of the height and the upstream distances from each boundary. The N, E, S, and W indications correspond to the northern, eastern, southern, and western boundaries, respectively.

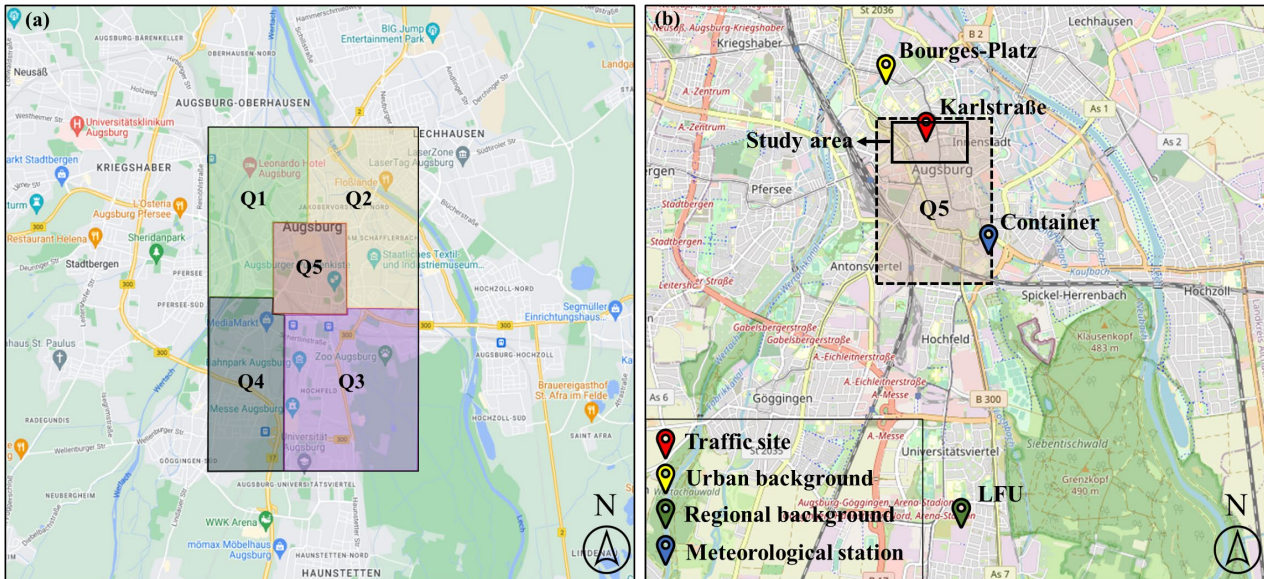


**Figure 1.** Surrounding environment containing the wider area of Augsburg with Q1–Q5 sub-domains (a), closeup of the case study area containing AQ sensors and meteorological station positions (b).

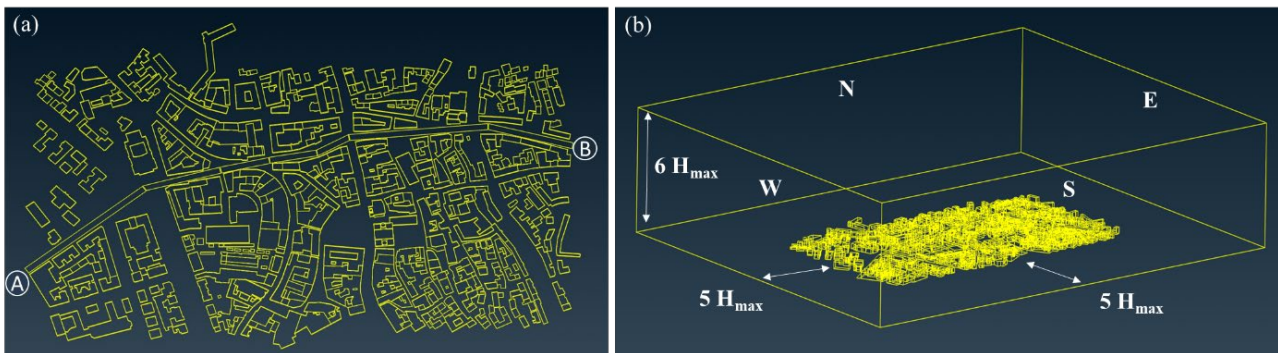


**Figure 2.** Top view of the digital model with emission sources (a) and computational domain dimensions (b).

## 2.2. Traffic Emissions

Emission rates for the three pollutants from traffic activity were used as input in the model. Average daily traffic volumes (ADTV) for different road IDs were used to calculate traffic emissions for September 2018. In Figure 1a, it is shown that the wider Augsburg area is divided into 5 sub-domains. The 4 sub-domains (Q1–Q4) concern suburban areas. In the Q5 area, where the case study area was located, traffic volumes typical of urban activity were given. To come up with hourly traffic activity of each one of the road IDs, the hourly deviation of the daily traffic volume was known and, therefore, applied to estimate the hourly traffic activity for every segment, representing sections of the road network of the city. In this way, the hourly traffic data helps to distinguish periods of maximum and minimum traffic activity in the city center. The COPERT Street software was employed to estimate traffic emissions for CO, PM, and NO<sub>x</sub> using the traffic activity data. To achieve high quality representation of the fleet characteristics of the area, information regarding the

vehicles registered in the city center of Augsburg for 2018 was used from the Federal Motor Transport Authority. Passenger cars comprised 73.6% of the fleet, LCVs 12.7%, HDT 5.6%, buses 0.6%, and motorcycles 7.5%. An average speed of 30 km/h was used, and the length of each road ID was known. The seven emission sources used in the model described in Section 2.1 consisted of a total of 10 different road IDs. Even though the most suitable solution for the representation of traffic activity in that specific street could have come from remote sensing, the approach used here provides satisfactory accuracy considering the fleet characteristics. Figure 3 shows the total emissions of the sources used in the CFD model for the three pollutants on the 15 September 2018 in kg/h. In the same figure, it is shown that during the first 4 h of the day (00:00–04:00), the emissions of all pollutants were decreasing, reaching the lowest rate between 03:00 and 04:00. Between 04:00 and 14:00, the daily hourly emission profile indicated a constant increase of emissions with an exception during 12:00–13:00. No morning peak could be recognized because the day selected for the simulation was a weekend day and the traffic emissions were typical of weekend period, with low emissions in the morning and high emissions during the afternoon with a distinguishable drop in the night period [23]. This work aims to provide high spatial resolution on the time scales examined, being one hour each time for this case, for a whole span of a 24-h cycle. The traffic emissions used in the model concern emissions from vehicles. During that hourly period, no significant coagulation phenomena in the case of PM can be considered in the time scale examined [24]. During this day, the highest emission rates collectively for the road IDs used appear during 13:00–14:00, with PM emitted at a rate of  $8.38 \times 10^{-3}$  kg/h,  $\text{NO}_x$  at  $4.1 \times 10^{-1}$  kg/h and CO at  $7.71 \times 10^{-1}$  kg/h, as displayed in Figure 3.

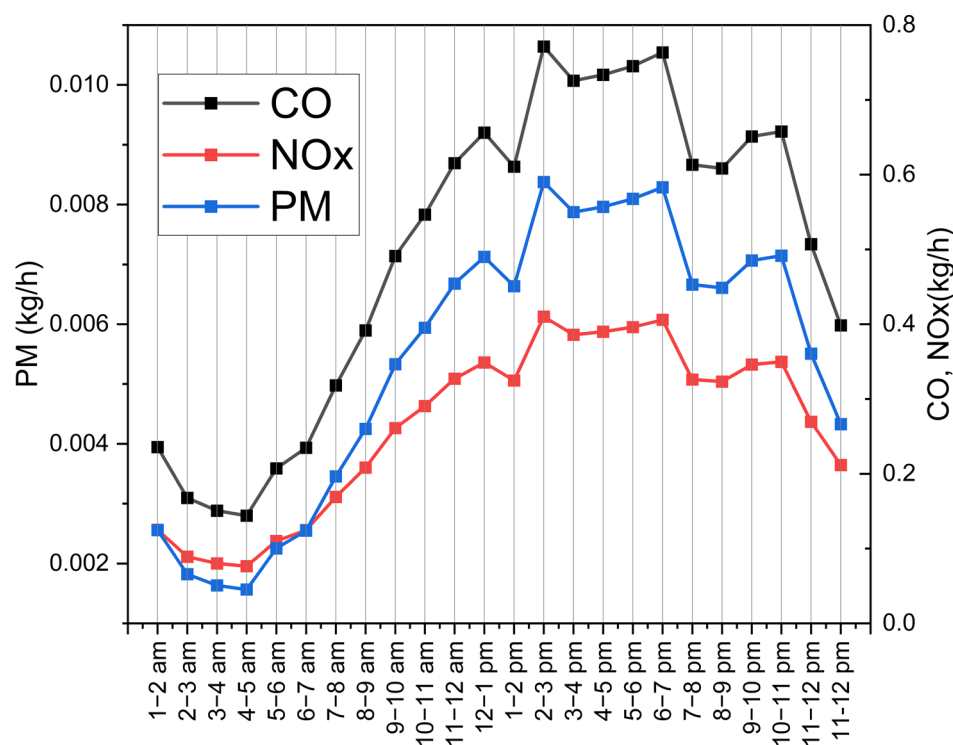


**Figure 3.** Traffic emissions from the sources included in the model during the daily simulated period on 15 September 2018.

### 2.3. Meteorological Conditions

An air quality model requires the use of meteorology of the area as an input during the simulated period. Wind speed and wind direction data were obtained from a sensor located on the southeastern side of the city center, 1.5 km away from the case study site, outside the urban fabric and unaffected by buildings, as shown in Figure 1b. The device

belonged to the smartAQnet network and sat at a height of 3 m. SmartAQnet is a sensor network operating in Augsburg, Germany [25]. The network is a hybrid of a small number of high-precision measurement stations established by government agencies and a large amount of mid- and low-cost sensors run collaboratively by citizens and researchers. There are more than 30 meteorological and aerosol properties observed in the network including temperature, air pressure, relative humidity, precipitation, wind speed, and wind direction. The observed area of the network was a rectangular area of about  $16 \times 16 \text{ km}^2$ , and a considerable portion of the sensors were located in an area of  $6 \times 4 \text{ km}^2$  that covered most of the Augsburg city center. Figure 4 demonstrates that prevailing winds during the simulated period were mostly of north-eastern and western direction. It was also shown that wind speed was low, ranging from 0.2 to 1.2 m/s. In this, 21% were between 0.2 and 0.4 m/s, 29% between 0.4 and 0.6 m/s, 13% in the range of 0.6–0.8 m/s and 0.8–1 m/s, and 24% between 1 and 1.2 m/s. So, 76% of the cases concerned calm wind conditions and can be explained by the low height of the installed device. The application of an atmospheric boundary layer profile on the model boundaries allowed for the correct development of the wind flow during the simulations, as described in Section 2.4.1.

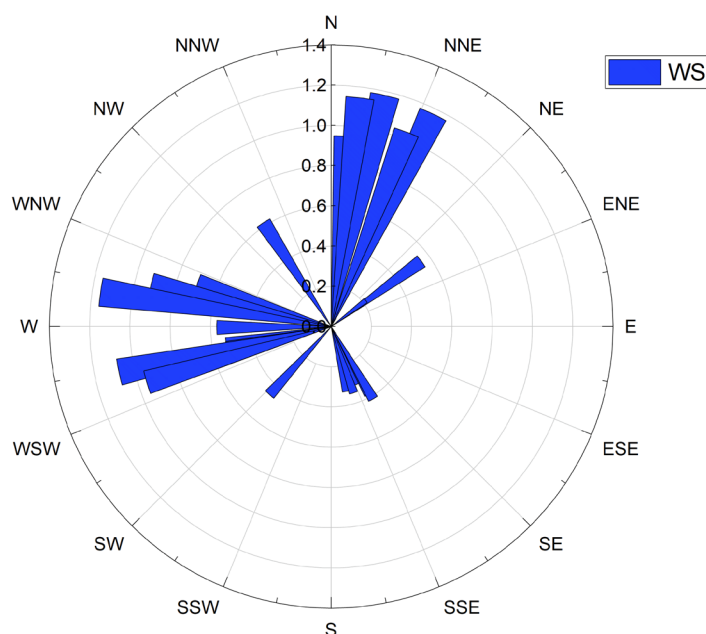


**Figure 4.** Meteorological conditions in the simulated area on 15 September 2018. Wind speed (m/s) and wind direction used in simulations.

## 2.4. CFD Model Setup

### 2.4.1. Numerical Model

The open-source CFD code OpenFOAM was implemented for the modelling of the pollutant dispersion. Due to the hourly temporal resolution of traffic emissions, meteorological data, and measurements, the cases were considered to be steady-state for every simulation performed. The steady-state Reynolds-averaged Navier–Stokes (RANS) approach was chosen for the simulations instead of a transient approach due to the constant conditions and the reduced computational cost [26]. The built-in numerical solver simpleFoam uses RANS equations to resolve the velocity field [27]. The passive scalar transport equation (Equation (1)) is included into the modified solver and compiled to the system, thus creating a solver that accounts for dispersion of passive pollutants [28–30].

$$\frac{\partial C}{\partial t} + \frac{\partial(\bar{u}_j C)}{\partial x_j} - \frac{\partial}{\partial x_j} \left( Def_{eff} \frac{\partial C}{\partial x_j} \right) = 0 \quad (1)$$

In Equation (1),  $D_{eff}$  is the sum of the turbulent diffusion coefficient term  $D_t$  and  $D_m$  that is the molecular diffusion one. Since, in the case of the pollutants in question, the molecular diffusivity does not influence the dispersion, and because the winds are considered of low velocity, the term  $D_m$  would not contribute to the dispersion. Bonifacio et al. (2014) [31] conducted numerical simulations for the dispersion of particles and because the molecular diffusion term of the particles was 9 orders of magnitude lower than the turbulent term, it was neglected in the model. Holmes and Morawska (2006) [24] performed a review on modelling capabilities of the dispersion of particles and pointed out that it is safe to model particle dispersion within a street environment without considering coagulation phenomena in short timescales. In the case of  $\text{NO}_x$ , the pollutant was regarded as a non-reactive pollutant, considering again the short timescale and that urban areas in the micro-scale are in neutral stability [16].

Equation (2) refers to the turbulent Schmidt number ( $Sc_t$ ). Using that equation and by setting the turbulent Schmidt number to 0.7 [32], the turbulent diffusion term  $D_t$  was computed. In this case, the predetermined kinematic viscosity of air in atmospheric conditions was  $1.5 \times 10^{-5} \text{ m}^2/\text{s}$ , set on the boundaries of the domain. The term  $\nu_t$  is the turbulent viscosity produced by Equation (2) in each timestep of the CFD simulation to characterize the air flow within the simulated domain.

$$Sc_t = \frac{\nu_t}{D_t} \quad (2)$$

The standard  $k-\varepsilon$  turbulence model was used for the RANS simulations [33,34]. Pan-tusheva et al. (2022) [22] demonstrated several types of turbulence models used in urban pollutant dispersion modelling with CFD and showed that 38% of the cases examined included the standard  $k-\varepsilon$ , clearly defining it as the most suitable turbulence model for these applications. As for the atmospheric velocity profile, Equation (3) refers to the profile set on the inlets of each case [35]. In Equation (3),  $u^*$  refers to the friction velocity,  $\kappa$  to the Von Karman constant valued at 0.41, and  $z_0$  is the aerodynamic roughness length at 0.25 m for a rough surface [36].

$$U(z) = \frac{u^*}{\kappa} \ln\left(\frac{z + z_0}{z}\right) \quad (3)$$

#### 2.4.2. Computational Mesh

The CFD model developed used a tetrahedral unstructured grid. The growth rate was 1.2 and the maximum skewness value was set to 0.9. Two different grids were developed for sensitivity analysis of the convergence criteria of the CFD simulation. The total amount of elements of each grid were 9 million cells for the medium mesh and 28 million cells for the fine mesh. The grid resolution for the medium mesh was set to 2 m for the buildings, 0.5 m for the emission sources, and 15 m on the boundaries. Respectively, the refinement for the fine mesh was 1 m for the buildings, 0.25 m for the sources, and 15 m on the boundaries. In Figure 5, the two grids are shown with a closeup at one of the buildings in each case, showcasing the difference between a refinement of 2 m and 1 m on the mesh developed.

To evaluate the two computational grids developed, simulations using the fine and medium grids were performed to determine if the convergence criteria were met. Both grids had acceptable convergence since the residuals on Table 1 were in the range of  $10^{-6}$  and  $10^{-7}$ , which is within the recommended range proposed [22]. No noticeable difference was observed in the residuals value when comparing the fine and medium grids, which would indicate one grid being more suitable than the other. Parameters such as velocity, TKE, epsilon, and pressure were examined for a representative period between 13:00 and 14:00 for the grid configurations. Table 1 shows the modelled values of the abovementioned variables at the location of the sensor for the medium and fine grid. For all the variables examined, the values calculated by the fine grid were all within the same order of magnitude as the coarser one with no significant deviation capable of producing substantially different outcomes. All simulations were performed using the same number



of processors on a computer node consisting of Intel(R) Core (TM) i9-10980XE @ 3.00 GHz CPUs. The medium grid took 651 min to compute and the fine one 2165. Eventually, the medium mesh was selected, given that it solved the cases about 3 times faster than the fine one, the residuals remained relatively constant, and the modelled parameters were all within the same order of magnitude with small deviations between them. After selecting the suitable mesh, the  $y^+$  dimensionless parameter, crucial for wall-bounded turbulent flows, was calculated for the buildings and the ground patches. Ariff et al. (2009) [37] mentioned that a range of  $30 < y^+ < 300$  is acceptable for regions where turbulent shear predominates. For the selected grid, the  $y^+$  for the buildings and the ground had an average value of 188 and 293, respectively, deeming the grid suitable for the current application.

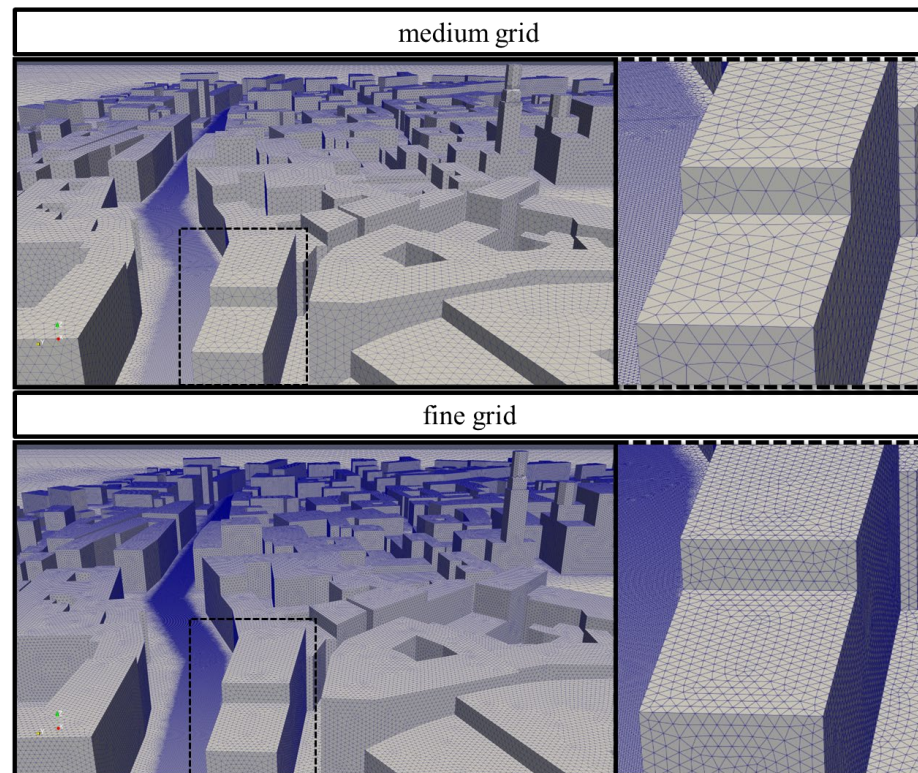


**Figure 5.** Comparison between the medium grid (9 million elements) and fine grid (28 million elements), focusing on a building with a refinement of 2 m for the medium and 1 m for the fine one.

**Table 1.** Scaled residuals of parameters of governing equations and simulated values at the sensor location for each computational mesh developed for this work for sensitivity analysis purposes.

| Mesh          | Medium                |                       |           | Fine                  |                       |           |
|---------------|-----------------------|-----------------------|-----------|-----------------------|-----------------------|-----------|
| Variable      | Residuals             | Value at Sensor       | Units     | Residuals             | Value at Sensor       | Units     |
| $U_x$         | $3.30 \times 10^{-7}$ | 0.25                  | m/s       | $3.20 \times 10^{-7}$ | 0.38                  | m/s       |
| $U_y$         | $7.10 \times 10^{-7}$ | 0.01                  | m/s       | $4.80 \times 10^{-7}$ | -0.01                 | m/s       |
| $U_z$         | $4.00 \times 10^{-6}$ | -0.05                 | m/s       | $3.50 \times 10^{-6}$ | -0.04                 | m/s       |
| $U$ magnitude | N/A                   | 0.25                  | m/s       | N/A                   | 0.38                  | m/s       |
| $p$           | $6.00 \times 10^{-7}$ | $-2.0 \times 10^{-1}$ | $m^2/s^2$ | $5.00 \times 10^{-7}$ | $-9.0 \times 10^{-2}$ | $m^2/s^2$ |
| $k$           | $2.00 \times 10^{-6}$ | $2.0 \times 10^{-4}$  | $m^2/s^2$ | $1.70 \times 10^{-6}$ | $1.2 \times 10^{-4}$  | $m^2/s^2$ |
| epsilon       | $2.80 \times 10^{-6}$ | $6.0 \times 10^{-4}$  | $m^2/s^3$ | $2.60 \times 10^{-6}$ | $2.0 \times 10^{-4}$  | $m^2/s^3$ |



### 3. Results

#### 3.1. CFD Parameters

The converged simulation provides values of the parameters calculated in the modelling process for every point of the computational grid. In this section, an analysis of the distribution of these parameters on a 2D section was performed and also the boundary conditions used in the OpenFOAM cases setup are described. Figure 6 depicts the distribution of the velocity magnitude  $U$ , the turbulent kinetic energy  $k$ , the dissipation of TKE  $\epsilon$ , and the relative pressure  $p$  along a YZ axis plane where the sensor was placed. The aspect ratio  $H/W$  of the height and the width of the street canyon was about 1, as shown in Figure 6a. In Figure 6a, the simulated wind velocity is shown in a frame on the YZ axis that reached a maximum height of 40 m. Wind velocity showed a direct dependency on the height following the velocity profile in Equation (3). The maximum estimated value of wind velocity reached about 3 m/s at the maximum height of the frame, and decreased values in lower heights. Inside the street canyon and between the two structures, the velocity was reduced because of the right building acting as a barrier to the air flow, shown on the right side of Figure 6. It is also shown that in the windward side of the canyon, the wind flow was also reduced. On the building's surface and on the ground, the velocity was zero according to the noSlip condition on OpenFOAM setup. In Figure 6d, it is shown that the kinematic pressure  $p$  was increased within the street canyon and especially on the leeward side of the left building. For incompressible flows, the pressure is divided by the density of air, therefore, the units are  $(m^2/s^2)$ . On the top-right side of the canyon, an area of low pressure was recognized. In Figure 6b, the turbulent kinetic energy  $k$  appears in lower values close to the ground and the buildings and it also follows a height-dependent profile. The boundary condition for buildings and ground was kqRWallFunction, providing a simple wrapper around the zero-gradient condition, which can be used for the turbulent kinetic energy. The TKE dissipation rate  $\epsilon$  was enhanced on the edges of the top side of the buildings (Figure 6c). In this case, the epsilonWallFunction was set as a boundary condition for the buildings and the ground. This boundary condition provides a wall constraint for epsilon and TKE's production contribution  $G$  (Equation (6)) that represents the transfer of kinetic energy from mean flow to turbulent fluctuations for low and high Reynolds number models. In Equation (4),  $\epsilon$  computed by the viscous sublayer assumptions used parameters such as the kinematic viscosity near wall ( $\nu_\omega$ ), the cell-corner weights ( $\omega$ ), turbulent kinetic energy ( $\kappa$ ), and the wall-normal distance ( $y$ ). In Equation (5),  $\epsilon$  is computed by the inertial sublayer assumptions with the addition of an empirical model constant ( $C_\mu$ ) and turbulent viscosity near wall ( $\nu_{\tau\omega}$ ).

$$\epsilon_{vis} = 2\omega\kappa \frac{\nu_\omega}{y^2} \tag{4}$$

$$\epsilon_{log} = \omega C_\mu \frac{\kappa^{\frac{3}{2}}}{\nu_{\tau\omega} y} \tag{5}$$

$$G = \omega(\nu_{\tau\omega} + \nu_\omega) \left| n \times (\nabla u)_f \right| C_\mu^{\frac{1}{4}} \frac{\sqrt{\kappa}}{\kappa y} \quad \text{if } y^+ \geq y_{lam}^+ \tag{6}$$

Additionally, with the analysis of the boundary conditions affecting the examined parameters, the order of magnitude of turbulent viscosity ratio produced by the model was examined. For incompressible flows, such as this case, the ratio was derived by dividing the calculated kinematic turbulent viscosity with the kinematic molecular viscosity described in Section 2.4.1. At the sensor location, close to the ground, the viscosity ratio was 400, within the range of 10–10,000 ratios observed in the literature when applying turbulent CFD modelling [38]. The analysis of this section shows the distribution of the governing parameters at the area of interest on a 2D section and how the boundary conditions set by the CFD model affect the values of the variables close to the ground and buildings. It

also is useful to point out the influence that these gradients have on the dispersion of the pollutant at the same area, as demonstrated in Section 3.2.

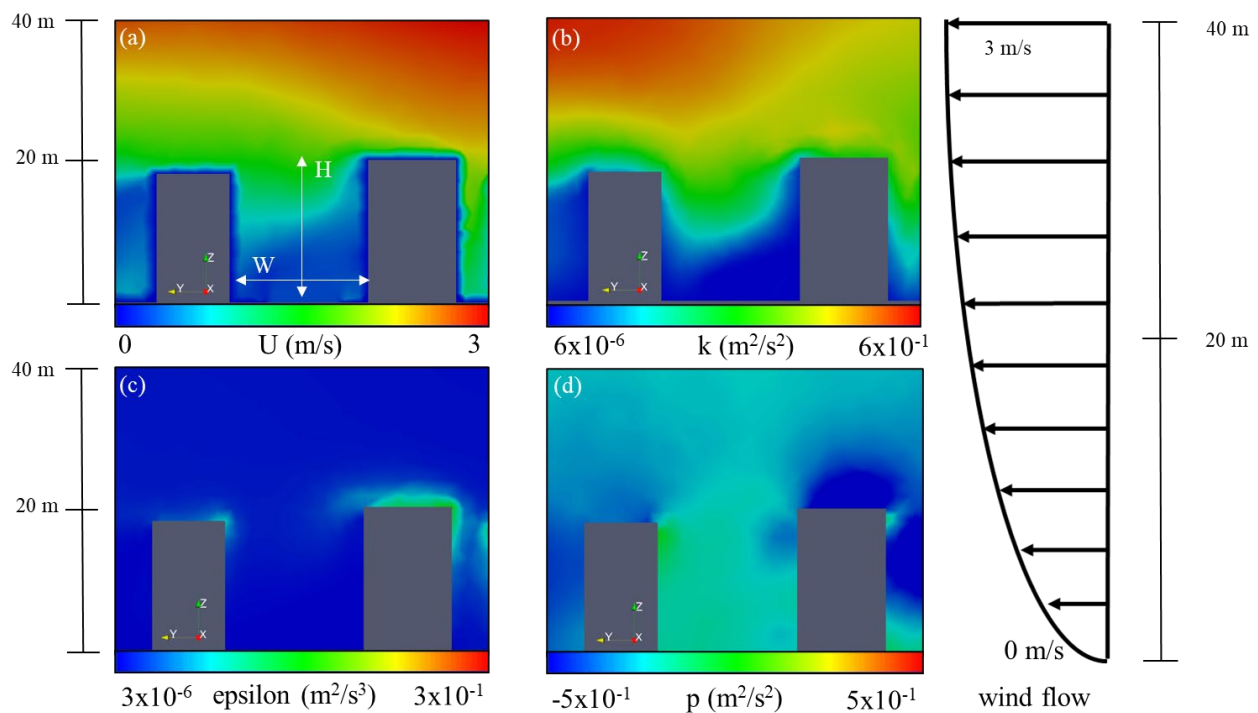


**Figure 6.** ZY plane at the AQ sensor location during 13:00–14:00. CFD variables calculated by OpenFOAM at the end of the RANS simulations, velocity magnitude  $U$  (a), turbulent kinetic energy  $k$  (b), TKE's dissipation rate  $\epsilon$  (c), and kinematic pressure  $p$  (d).

### 3.2. Pollutant Concentration at the Area of Interest Pollutant Spatial Distribution

Figure 7a shows the  $\text{NO}_x$  concentrations during 13:00–14:00 for the whole modelling domain on an XY plane. The plane stands at  $z = 2.5$  m, at the height where the air quality sensor is located. The selected time represents the highest emission scenario for the simulated 24-h period described in Section 2.2. Figure 7a shows  $\text{NO}_x$  concentrations in the range of 0–75  $\mu\text{g}/\text{m}^3$ . It can be seen that in the area where the sensor is situated, depicted by the black pin, the concentration of the pollutants is higher compared to the other sides. This is explained due to the fact that there is contribution of vehicles coming to that area of the main artery from other roads, increasing the traffic activity, and resulting in higher calculated emissions. The simulated results also show that the sensor deployed in that area was placed correctly, in a position where high concentrations were observed, meaning it can capture representative pollutant indications. The dashed line shows the cut section on which the analysis for Figure 7b is made.

Figure 7b shows the distribution of pollutant concentration on a 2D plane, at the same area as the analysis of Section 3.1. Low velocity values at areas shown on Figure 5 are directly related to higher levels of pollutant concentration in Figure 7b. In Figure 7b, in the area where the pollutant dispersion is enhanced, the TKE appears in decreased values (Figure 6b), so a reversal analogy is recognized between the two variables. No direct association can be made between the pollutant and  $\epsilon$  in Figure 6c because the pollutant does not reach that height in great concentrations to identify any visible relationship. In Figure 7b the pollutant is depicted in higher concentrations close to the windward area, demonstrating a direct association between low pressure and higher pollution levels as seen in Figure 6d. Su et al. (2019) [11] examined the velocity magnitude and turbulent kinetic energy distribution on a 2D plane at the point of interest of the CFD simulations performed in an idealized street canyon. The aspect ratio between the height of the building

and the width of the area was  $H/W = 1$ . An analysis on the effect that these parameters have on the pollutant dispersion demonstrated that the pollutant was concentrated in higher values in areas where TKE was decreased. Accordingly, in areas where velocity was high, pollutant concentration was also decreased. The analysis performed in this work also indicates that high pollutant concentration is related to low pressure and low turbulent kinetic energy areas. It also shows that higher wind velocity is responsible for low concentrations, implying that intense wind helps decongest the contaminant.

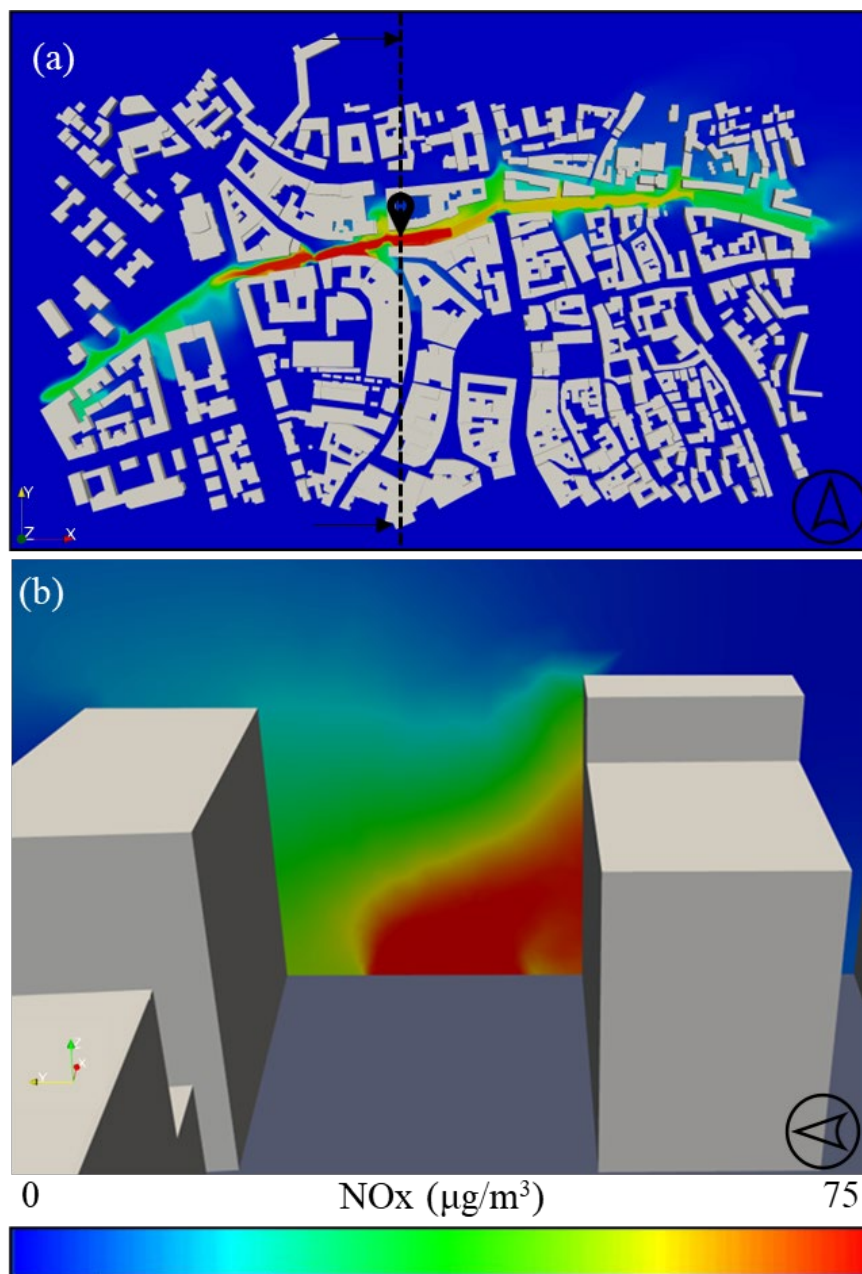


**Figure 7.** NOx concentrations during 13:00–14:00, 15 September 2018, at  $z = 2.5$  m (a) and pollutant distribution on a YZ plane (b).

To demonstrate the high spatial resolution results the CFD model produces, five different concentration values of NO<sub>x</sub> were extracted at an area of  $60 \times 20$  m<sup>2</sup> around the AQ sensor location, as seen in Figure 8. The points were selected as representative of pavement locations, at the height of the AQ measuring station. Figure 8 shows the deviation between the different points and the simulated value at the sensor coordinates (point 0).

The divergence percentages apply for both gaseous pollutants because the spatial diffusion simulated by the model is the same. For the area concerning the analysis, a deviation of up to +50% and down to −18% can be identified between points 1–5 and point 0. This shows that the application of a CFD model for assessing urban air quality can produce pollutant concentration fields that vary in values at the street scale. In this way, it can be used to directly quantify the urban population's exposure to the contaminants in specific locations inside a street canyon and to recognize areas and points where the pollutant can be congested, according to the urban architecture planning, and to assess the impact of potential measures applied aiming to decrease exposure of people to pollutants.

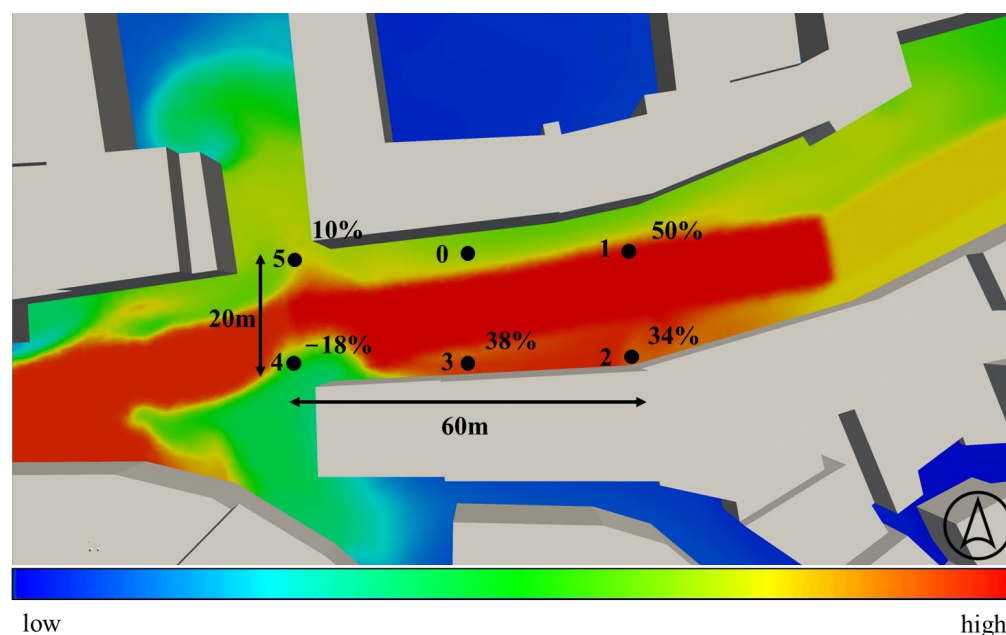


**Figure 8.** Spatial resolution analysis at  $z = 2.5$  m. Six different pollutant concentrations taken from each point and their corresponding deviation from the AQ station at point 0 at an area of  $20 \times 60$  m<sup>2</sup>.

Veratti et al. (2020) [39] produced high-resolution concentration maps of NO<sub>x</sub> in the city of Modena on a  $6 \times 6$  km<sup>2</sup> area using WRF-Chem and the PMSS model. For the traffic station area, the concentrations modelled reached a maximum of  $175 \mu\text{g}/\text{m}^3$  with a resolution of 4 m. Barbero et al. (2021) [40] also used hybrid modelling to simulate traffic emissions dispersion in the city of Rome with a grid resolution of 4 m. The models used for the coupling method were FARM and PMSS. Sanchez et al. (2017) [16] demonstrated a spatial distribution of NO<sub>x</sub> in Madrid's center ranging from 0 to  $225 \mu\text{g}/\text{m}^3$  by applying CFD modelling. The size of the computational domain was  $1.3 \times 1.3$  km<sup>2</sup> and the resolution of the resulting concentrations was under 1 m. According to the concentration maps developed, in areas of  $50 \times 50$  m<sup>2</sup>, a deviation of  $\pm 25\%$  among the concentration values can be recognized. The analysis performed by the authors is compatible with the findings of this model, given that in roughly the same area, the same range of deviation can be seen. The demonstration of the high range of deviated concentrations within close proximity to a fixed point shows the capabilities of this CFD model to capture high resolution concentrations related to sources in the street scale with a grid resolution of under 0.5 m.

### 3.3. Daily Cycle and Comparison with Measurements

In order to validate the model's performance, comparisons with a high-precision air quality sensor were performed for each hour of the day. The AQ sensor was located across the main road artery of the area, and the objective was to find the correlation between the measured NO<sub>x</sub>, CO, and PM with the simulation. To accurately compare the simulated findings with observations, concentrations from an urban background station

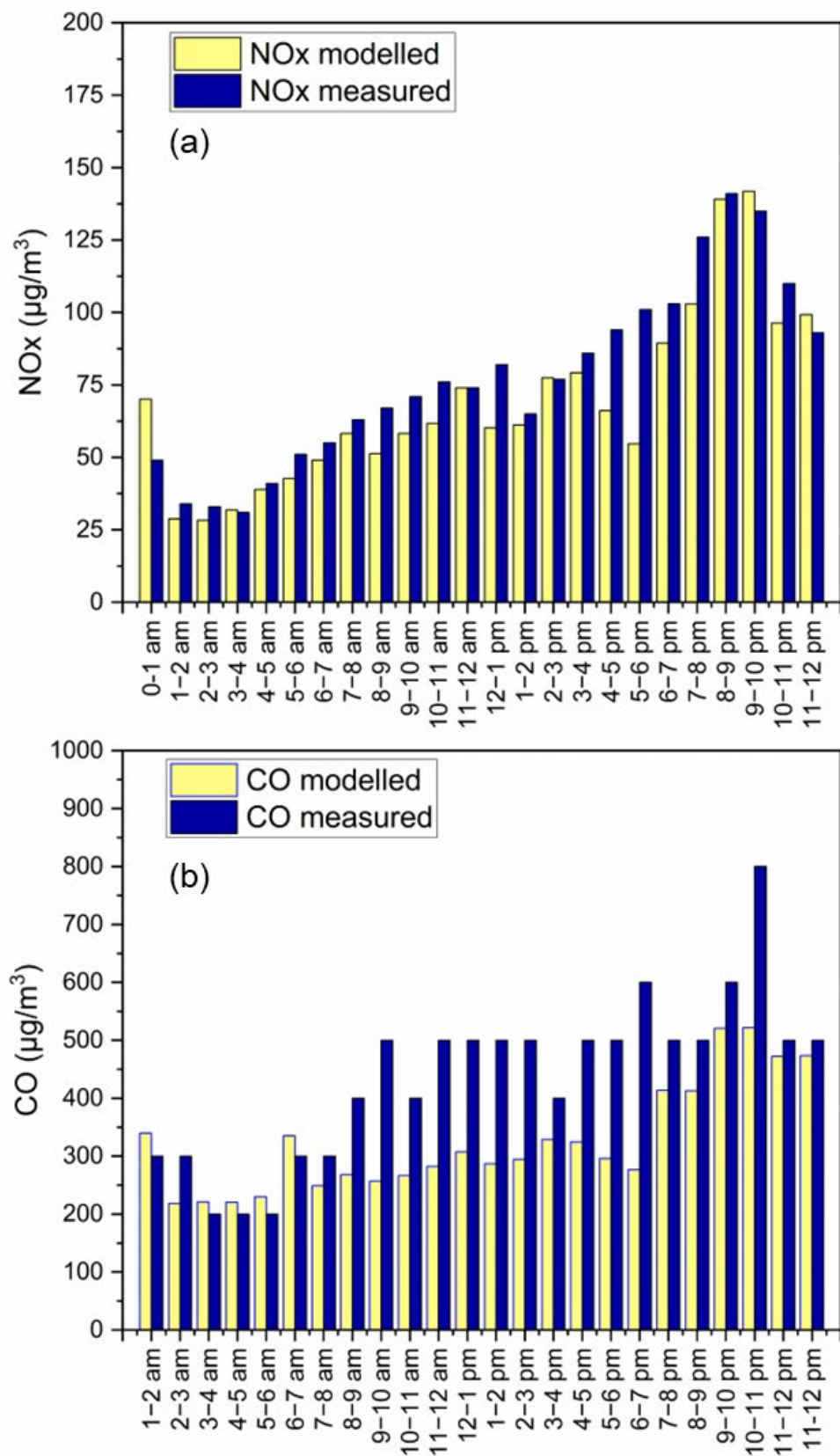


were added to the CFD outputs. The addition of background concentrations helps to construct a comprehensive air quality network that assesses overall air quality of the area, with focus on the street scale depicted by the CFD results. The urban background station was located at the northern side of the test case area, at Bourges-Platz, 1 km away from the study area. This was performed in the case of  $\text{NO}_x$  by adding  $\text{NO} + \text{NO}_2$  concentrations to come up with total  $\text{NO}_x$  [16], and for the case of  $\text{PM}_{10}$  concentrations. No information on CO concentrations was given from that station, so CO concentrations from a regional background station at LFU (Figure 1b) were used.

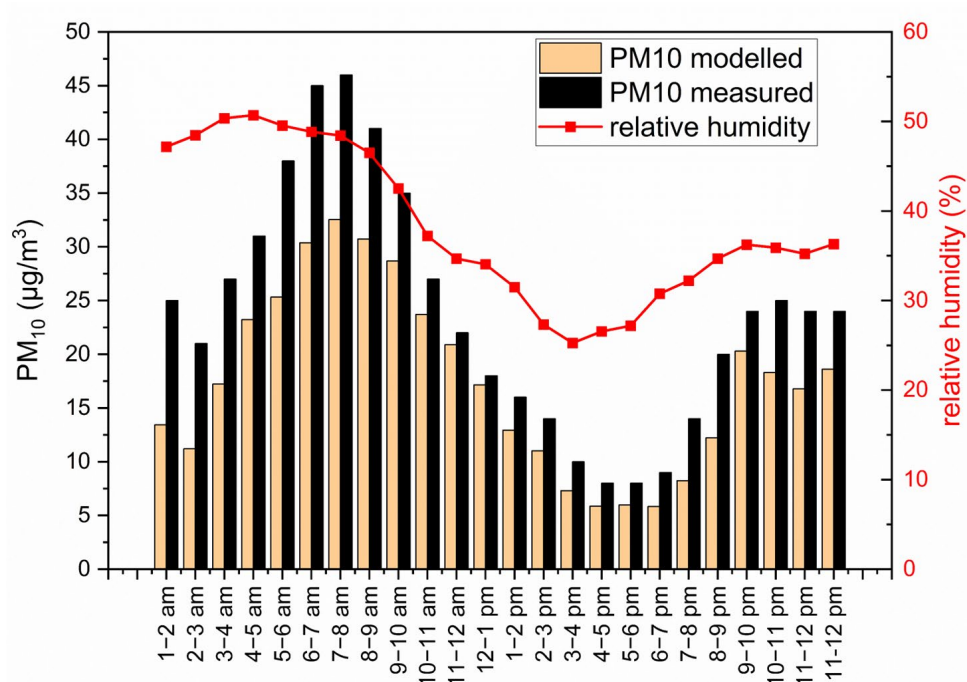
Figure 9a shows the comparison between the predicted and observed  $\text{NO}_x$  concentrations at the location of the AQ station. The average daily absolute deviation between the modelled concentrations and the measurements was 11% and they shared a coefficient  $r^2$  equal with 0.82. It is clear that the modelled  $\text{NO}_x$  concentration on the receptor point depicts low values in the morning hours and peaks during noon and the afternoon hours, until 22:00 when the concentrations drop. The same behavior was also noticed with the measured values, with low concentrations in the morning, high during the afternoon, and a drop after 22:00. In Figure 9b, for the case of CO, it is shown that all the simulated values lay within the same range with measurements. An increasing trend of the CFD values can be recognized for CO, also with low values in the morning and two peaks during 14:00–15:00 and 21:00–22:00. The CO concentrations showed a decrease in value after 22:00, both for the modelled and the observed ones. The CO indications from the station were found to be quantized with a sensitivity of  $100 \mu\text{g}/\text{m}^3$ . This adds to the unreliability of CO measurements. Considering this, the modelled concentrations provide higher accuracy of concentration, with a resolution of several orders of magnitude lower than the measured ones. The total daily divergence of the modelled CO values from the measured ones was 26% and an established coefficient  $r^2$  equal with 0.54. Olivardia et al. (2019) [41] compared CFD-generated  $\text{NO}_2$  and NO values with observations for a one-day period during August 2010 at Osaka City, Japan. During that 24-h period, the average daily deviation from measurements was approximately 28% for  $\text{NO}_2$  and 23% for NO. The findings of this work's model, collectively for  $\text{NO}_x$ , generated concentrations that deviated less from measurements compared to the abovementioned work, showcasing an example of good performance.

Figure 10 demonstrates the modelled and observed particle concentrations, along with relative humidity levels during the 24-h period. In that graph, a peak in particle concentrations can be observed during 03:00–10:00, that cannot be attributed to traffic activity since it does not follow the trends of the emissions. One of the reasons for that, as it can be seen in Figure 10, would be that there is high relative humidity in that area, as taken from smartAQnet indications. Schäfer et al. (2014) [42] examined the role of meteorological conditions on pollutants in Augsburg and pointed out that high PM concentrations were related to low wind speeds, high relative humidity, and low mixing layer heights. The average daily deviation between model and observations was 27% with an  $r^2 = 0.91$ . Overall, for this work the modelled values were all within the same range as measurements with an accepted deviation and seemed to follow satisfactory trends that appeared in observations.

The analysis of this section shows that the CFD model developed can follow the trends influenced by traffic activity, as seen during this 24-h period, with outputs in the same range as measurements and accepted deviations for the case of the three pollutants examined. Particularly for the case of carbon monoxide, the model provides higher accuracy as the concentrations of the pollutant produced were not quantized, as noticed for the station's indications. A more thorough analysis on the results using statistical parameters for all the pollutants for the evaluation of the model is performed in Section 3.4.



**Figure 9.** Comparison between the measured and simulated values for a 24-h cycle on the 15 September 2018 for NO<sub>x</sub> (a) and CO (b).



**Figure 10.** Comparison between the measured and simulated particulate matter concentrations (left Y axis). Relative humidity for the corresponding time period (right Y axis).

### 3.4. Validation Metrics for CFD Models

To accurately validate findings of CFD models with observations, statistical metrics were used to assess the performance of the model [43]. The normalized concentrations both for the predicted (P) and the observed (O) values were calculated using Equation (7) where C is the calculated concentration,  $U_{ref}$  is the wind speed, Q the emission rate, and H is the average building height of the study area. In Table 2, the statistical metrics of this work and the accepted ranges according to literature are shown.

$$C^* = \frac{CU_{ref}H^2}{Q} \tag{7}$$

**Table 2.** Validation metrics for particulate matter, CO, and NO<sub>x</sub> for the evaluation of the modelled outputs.

|      | PM   | CO   | NO <sub>x</sub> | Ideal Model | Accepted Range      |
|------|------|------|-----------------|-------------|---------------------|
| FAC2 | 1.00 | 0.96 | 0.96            | 1           | ≥0.5 [44]           |
| FB   | 0.30 | 0.26 | 0.10            | 0           | 0.3 ≤ FB ≤ 0.3 [45] |
| MG   | 1.38 | 1.30 | 1.12            | 1           | 0.7 ≤ MG ≤ 1.3 [44] |
| NMSE | 0.21 | 0.16 | 0.04            | 0           | ≤1.5 [45]           |

All the statistical metrics were calculated separately for each pollutant every hour using the corresponding wind speeds in Equation (7). At the end, the average metric from all the cases is demonstrated in Table 2. In the case of CO and NO<sub>x</sub>, the parameters calculated were in the accepted range. For CO, all the indicators were accepted except from MG that; even though it did not deviate greatly from the criteria, it did not appear to lie within the accepted values. Noticeable for the three pollutants is that they appear to give a minor underprediction. An MG > 1 leads to that conclusion for all the cases. Pantusheva et al. (2022) [22] pointed out that 20% of the total reviewed papers studied that concerned pollutant dispersion using CFD do not use any formal verification means to assess their results. For this work, given the fact that all the predicted values lie within the same range with observations and that the vast majority of the statistical indicators

that assess the simulated results are accepted, the CFD model performs well and provides reliable predicted pollutant concentrations. This means that the concentrations produced in the area of interest accurately represent the pollution condition in the city with a focus on street scale pollution created by traffic emissions.

#### 4. Conclusions

Monitoring air quality in urban environments has become more crucial than ever and modern tools provide the opportunity to construct high-precision digital networks for any given city. This work demonstrated the development of such a highly accurate 3D model, by producing concentration maps for CO, PM, and NO<sub>x</sub> at a high traffic activity urban area. CFD modelling was applied for the dispersion of the pollutants from vehicular activity during a 24-h period. The open-source CFD code OpenFOAM was implemented for the solving of the case. The model was evaluated using indications from a highly precise AQ station on that area. The predicted values followed the trends that appear with the urban pollution indications, influenced greatly by traffic. This work showed that the solver developed for this application can successfully simulate the dispersion both of gaseous and particulate pollutants at the street scale, by producing concentrations that deviate 11–27% from measurements and regression coefficients calculated between 0.54 and 0.91 during the day.

A highly spatially accurate model such as this can be used to analyze pollutant distribution in areas where air quality stations indicate steady pollution levels to assess the representativeness of the measurement across the street canyon. This is why this work focused on exhibiting variability in concentrations produced at the street canyon scale, highlighting the capability of the model to recognize areas of low and high contamination within a constrained area, with focus on phenomena directly influenced by traffic in the appropriate timescales. A CFD model could also take advantage of the accurate outputs, as demonstrated in this work, to provide calibration and correct positioning of an air quality sensor network. Future research should focus on using highly accurate models such as this, including various other sources of emissions, in combination with measurements to provide a full system for air quality assessment suitable for smart cities applications.

**Author Contributions:** Conceptualization, G.I., L.N. and T.R.; methodology, G.I. and L.N.; software, G.I.; validation, G.I. and L.N.; formal analysis, G.I. and L.N.; investigation, G.I. and L.N.; resources, C.L., P.T. and T.R.; data curation, G.I.; writing—original draft preparation, G.I. and L.N.; writing—review and editing, G.I. and L.N.; visualization, G.I.; supervision, L.N.; project administration, L.N.; funding acquisition, L.N. All authors have read and agreed to the published version of the manuscript.

**Funding:** The work is funded by the Helmholtz Association of German Research Centres, through the GRACE foundation under funding number 51. The work is related to the HEPTA project, concerning the “Air Quality in Smart Cities” topic.

**Institutional Review Board Statement:** Not applicable.

**Informed Consent Statement:** Not applicable.

**Data Availability Statement:** Data are contained within the article.

**Acknowledgments:** The contribution of Ulrich Uhrner and Raphael Reifeltshammer of the University of GRAZ is acknowledged for providing traffic activity data. OPENFOAM® is a registered trademark of OpenCFD Limited, producer and distributor of the OpenFOAM software v21106 via [www.openfoam.com](http://www.openfoam.com) (accessed on 15 October 2021).

**Conflicts of Interest:** The authors declare no conflicts of interest.



## References

1. Zhang, K.; Batterman, S. Air pollution and health risks due to vehicle traffic. *Sci. Total Environ.* **2013**, *450–451*, 307–316. [[CrossRef](#)] [[PubMed](#)]
2. Ju, K.; Lu, L.; Wang, W.; Chen, T.; Yang, C.; Zhang, E.; Xu, Z.; Li, S.; Song, J.; Pan, J.; et al. Causal effects of air pollution on mental health among Adults—An exploration of susceptible populations and role of physical activity based on a longitudinal nationwide cohort in China. *Environ. Res.* **2022**, *217*, 114761. [[CrossRef](#)] [[PubMed](#)]
3. Reşitoğlu, I.A.; Altınışık, K.; Keskin, A. The pollutant emissions from diesel-engine vehicles and exhaust aftertreatment systems. *Clean Technol. Environ. Policy* **2015**, *17*, 15–27. [[CrossRef](#)]
4. Li, F.; Schnelle-Kreis, J.; Cyrus, J.; Karg, E.; Gu, J.; Abbaszade, G.; Orasche, J.; Peters, A.; Zimmermann, R. Organic speciation of ambient quasi-ultrafine particulate matter (PM<sub>0.36</sub>) in Augsburg, Germany: Seasonal variability and source apportionment. *Sci. Total Environ.* **2018**, *615*, 828–837. [[CrossRef](#)] [[PubMed](#)]
5. Angatha, R.K.; Mehar, A. Impact of Traffic on Carbon Monoxide Concentrations Near Urban Road Mid-Blocks. *J. Inst. Eng. Ser. A* **2020**, *101*, 713–722. [[CrossRef](#)]
6. Grewe, V.; Dahlmann, K.; Matthes, S.; Steinbrecht, W. Attributing ozone to NO<sub>x</sub> emissions: Implications for climate mitigation measures. *Atmos. Environ.* **2012**, *59*, 102–107. [[CrossRef](#)]
7. Chen, R.; Pan, G.; Zhang, Y.; Xu, Q.; Zeng, G.; Xu, X.; Chen, B.; Kan, H. Ambient carbon monoxide and daily mortality in three Chinese cities: The China Air Pollution and Health Effects Study (CAPEs). *Sci. Total Environ.* **2011**, *409*, 4923–4928. [[CrossRef](#)]
8. Yazid AW, M.; Sidik nor, A.C.; Salim, S.M.; Saqr, K.M. A review on the flow structure and pollutant dispersion in urban street canyons for urban planning strategies. *Simulation* **2014**, *90*, 892–916. [[CrossRef](#)]
9. Tee, C.; Ng, K.E.Y.; Xu, G. Analysis of transport methodologies for pollutant dispersion modelling in urban environments. *J. Environ. Chem. Eng.* **2020**, *8*, 103937. [[CrossRef](#)]
10. Montazeri, H.; Blocken, B. CFD simulation of wind-induced pressure coefficients on buildings with and without balconies: Validation and sensitivity analysis. *Build. Environ.* **2013**, *60*, 137–149. [[CrossRef](#)]
11. Su, J.; Wang, L.; Gu, Z.; Song, M.; Cao, Z. Effects of real trees and their structure on pollutant dispersion and flow field in an idealized street canyon. *Atmos. Pollut. Res.* **2019**, *10*, 1699–1710. [[CrossRef](#)]
12. Fernández-Pacheco, V.M.; Álvarez-Álvarez, E.; Blanco-Marigorta, E.; Ackermann, T. CFD model to study PM 10 dispersion in large-scale open spaces. *Sci. Rep.* **2023**, *13*, 5966. [[CrossRef](#)]
13. Toscano, D.; Marro, M.; Mele, B.; Murena, F.; Salizzoni, P. Assessment of the impact of gaseous ship emissions in ports using physical and numerical models: The case of Naples. *Build. Environ.* **2021**, *196*, 107812. [[CrossRef](#)]
14. Sonia Oppo, W.; Karl, M.; Boikos, C.; Otto Paul, M. (Eds.) *THE SCIPPER Project Shipping Contributions to Inland Pollution Push for the Enforcement of Regulations Deliverable Title Shipping Emissions Contribution to Port and Neighbouring Urban Areas Dissemination Level (\*) Public (PU)*; Helmholtz-Zentrum Hereon: Geesthacht, Germany, 2023.
15. Lauriks, T.; Longo, R.; Baetens, D.; Derudi, M.; Parente, A.; Bellemans, A.; van Beeck, J.; Denys, S. Application of Improved CFD Modeling for Prediction and Mitigation of Traffic-Related Air Pollution Hotspots in a Realistic Urban Street. *Atmos. Environ.* **2021**, *246*, 118127. [[CrossRef](#)]
16. Sanchez, B.; Santiago, J.L.; Martilli, A.; Martin, F.; Borge, R.; Quaassdorff, C.; de la Paz, D. Modelling NO<sub>x</sub> concentrations through CFD-RANS in an urban hot-spot using high resolution traffic emissions and meteorology from a mesoscale model. *Atmos. Environ.* **2017**, *163*, 155–165. [[CrossRef](#)]
17. Rivas, E.; Santiago, J.L.; Lechón, Y.; Martín, F.; Ariño, A.; Pons, J.J.; Santamaría, J.M. CFD modelling of air quality in Pamplona City (Spain): Assessment, stations spatial representativeness and health impacts valuation. *Sci. Total Environ.* **2019**, *649*, 1362–1380. [[CrossRef](#)] [[PubMed](#)]
18. Akhatova, A.; Kassymov, A.; Kazmaganbetova, M.; Rojas-Solórzano, L. CFD Simulation of the Dispersion of Exhaust Gases in a Traffic Loaded Street of Astana, Kazakhstan. *J. Urban Environ. Eng.* **2015**, *9*, 158–167. [[CrossRef](#)]
19. Blocken, B. Computational Fluid Dynamics for urban physics: Importance, scales, possibilities, limitations and ten tips and tricks towards accurate and reliable simulations. *Build. Environ.* **2015**, *91*, 219–245. [[CrossRef](#)]
20. Zheng, X.; Montazeri, H.; Blocken, B. Large-eddy simulation of pollutant dispersion in generic urban street canyons: Guidelines for domain size. *J. Wind Eng. Ind. Aerodyn.* **2021**, *211*, 104527. [[CrossRef](#)]
21. Tominaga, Y.; Mochida, A.; Yoshie, R.; Kataoka, H.; Nozu, T.; Yoshikawa, M.; Shirasawa, T. AIJ guidelines for practical applications of CFD to pedestrian wind environment around buildings. *J. Wind Eng. Ind. Aerodyn.* **2008**, *96*, 1749–1761. [[CrossRef](#)]
22. Pantusheva, M.; Mitkov, R.; Hristov, P.O.; Petrova-Antonova, D. Air Pollution Dispersion Modelling in Urban Environment Using CFD: A Systematic Review. *Atmosphere* **2022**, *13*, 1640. [[CrossRef](#)]
23. Naiudomthum, S.; Winijkul, E.; Sirisubtawee, S. Near Real-Time Spatial and Temporal Distribution of Traffic Emissions in Bangkok Using Google Maps Application Program Interface. *Atmosphere* **2022**, *13*, 1803. [[CrossRef](#)]
24. Holmes, N.S.; Morawska, L. A review of dispersion modelling and its application to the dispersion of particles: An overview of different dispersion models available. *Atmos. Environ.* **2006**, *40*, 5902–5928. [[CrossRef](#)]
25. Kowalski, M.; Hank, M.; Kusch, T.; Cyrus, J. Smart Air Quality Network-Network Planning Phase 1/2 Deployment of Scientific Scouts (EDM80NEPH, GRIMM) and Reference Devices OPC (EDM164, GRIMM) Augsburg, Bayern. 2018. Available online: <https://www.smartaq.net/> (accessed on 19 October 2021).

26. Jon, K.S.; Huang, Y.-D.; Sin, C.H.; Cui, P.-Y.; Luo, Y. Influence of wind direction on the ventilation and pollutant dispersion in different 3D street canyon configurations: Numerical simulation and wind-tunnel experiment. *Environ. Sci. Pollut. Res.* **2023**, *30*, 31647–31675. [[CrossRef](#)] [[PubMed](#)]
27. Peralta, C.; Nugusse, H.; Kokilavani, S.P.; Schmidt, J.; Stoevesandt, B. Validation of the simpleFoam (RANS) solver for the atmospheric boundary layer in complex terrain. *ITM Web Conf.* **2014**, *2*, 01002. [[CrossRef](#)]
28. Elfverson, D.; Lejon, C. Use and scalability of openfoam for wind fields and pollution dispersion with building-and ground-resolving topography. *Atmosphere* **2021**, *12*, 1124. [[CrossRef](#)]
29. Miao, Y.; Liu, S.; Zheng, Y.; Wang, S.; Li, Y. Numerical study of traffic pollutant dispersion within different street canyon configurations. *Adv. Meteorol.* **2014**, *2014*, 458671. [[CrossRef](#)]
30. Rapkos, N.; Weigelt, A.; Beecken, J.; Ntziachristos, L. Method to identify fuel sulphur content (FSC) violations of ongoing vessels using CFD modelling. *Atmos. Environ.* **2023**, *309*, 119912. [[CrossRef](#)]
31. Bonifacio, H.F.; Maghirang, R.G.; Glasgow, L.A. Numerical simulation of transport of particles emitted from ground-level area source using AERMOD and CFD. *Eng. Appl. Comput. Fluid Mech.* **2014**, *8*, 488–502. [[CrossRef](#)]
32. Tominaga, Y.; Stathopoulos, T. Turbulent Schmidt numbers for CFD analysis with various types of flowfield. *Atmos. Environ.* **2007**, *41*, 8091–8099. [[CrossRef](#)]
33. Amorim, J.H.; Rodrigues, V.; Tavares, R.; Valente, J.; Borrego, C. CFD modelling of the aerodynamic effect of trees on urban air pollution dispersion. *Sci. Total Environ.* **2013**, *461–462*, 541–551. [[CrossRef](#)] [[PubMed](#)]
34. Santiago, J.L.; Martín, F.; Martilli, A. A computational fluid dynamic modelling approach to assess the representativeness of urban monitoring stations. *Sci. Total Environ.* **2013**, *454–455*, 61–72. [[CrossRef](#)] [[PubMed](#)]
35. Yang, Y.; Gu, M.; Chen, S.; Jin, X. New inflow boundary conditions for modelling the neutral equilibrium atmospheric boundary layer in computational wind engineering. *J. Wind Eng. Ind. Aerodyn.* **2009**, *97*, 88–95. [[CrossRef](#)]
36. Irwan Ramli, N.; Idris Ali, M.; Saad, H. Estimation of the Roughness Length (zo) in Malaysia using Satellite Image Earthquake Evaluation of Economical Aspects to Implement Seismic Design for New Reinforced Concrete Buildings in Malaysia View Project. 2009. Available online: <https://www.researchgate.net/publication/267769103> (accessed on 20 December 2022).
37. Ariff, M.; Salim, S.M.; Cheong, S. Wall y+ Approach for Dealing with Turbulent Flow over a Surface Mounted Cube: Part 1-Low Reynolds Number. In Proceedings of the 7th International Conference on Computational Heat and Mass Transfer, Istanbul, Turkey, 18–22 July 2009.
38. Acarer, S. Critical study of the effects and numerical simulations of boundary layer transition in lift-based wind turbines at moderate Reynolds numbers. *J. Renew. Sustain. Energy* **2020**, *12*, 063309. [[CrossRef](#)]
39. Veratti, G.; Fabbi, S.; Bigi, A.; Lupascu, A.; Tinarelli, G.; Teggi, S.; Brusasca, G.; Butler, T.M.; Ghermandi, G. Towards the coupling of a chemical transport model with a micro-scale Lagrangian modelling system for evaluation of urban NOx levels in a European hotspot. *Atmos. Environ.* **2020**, *223*, 117285. [[CrossRef](#)]
40. Barbero, D.; Tinarelli, G.; Silibello, C.; Nanni, A.; Gariazzo, C.; Stafoggia, M.; Viegi, G.; Ancona, C.; Angelini, P.; Argentini, S.; et al. A microscale hybrid modelling system to assess the air quality over a large portion of a large European city. *Atmos. Environ.* **2021**, *264*, 118656. [[CrossRef](#)]
41. Olivardia, F.G.G.; Zhang, Q.; Matsuo, T.; Shimadera, H.; Kondo, A. Analysis of pollutant dispersion in a realistic urban street canyon using coupled CFD and chemical reaction modeling. *Atmosphere* **2019**, *10*, 479. [[CrossRef](#)]
42. Schäfer, K.; Elsasser, M.; Arteaga-Salas, J.M.; Gu, J.; Pitz, M.; Schnelle-Kreis, J.; Cyrus, J.; Emeis, S.; Prevot AS, H.; Zimmermann, R. Meteorological conditions for air pollution Atmospheric Chemistry and Physics Source apportionment and the role of meteorological conditions in the assessment of air pollution exposure due to urban emissions Meteorological conditions for air pollution. *Atmos. Chem. Phys. Discuss.* **2014**, *14*, 2235–2275. [[CrossRef](#)]
43. Schatzmann, M.; Olesen, H.R. *COST 732 Model Evaluation Case Studies: Approach and Results VIEW Project*; COST: Brussels, Belgium, 2010; pp. 380–384. Available online: <https://www.researchgate.net/publication/257762245> (accessed on 15 November 2022).
44. Di Sabatino, S.; Buccolieri, R.; Pulvirenti, B.; Britter, R. Simulations of pollutant dispersion within idealised urban-type geometries with CFD and integral models. *Atmos. Environ.* **2007**, *41*, 8316–8329. [[CrossRef](#)]
45. Goricsán, I.; Balczó, M.; Balogh, M.; Czáder, K.; Rákai, A.; Tonkó, C. Simulation of flow in an idealised city using various CFD codes. *Int. J. Environ. Pollut.* **2011**, *44*, 359–367. [[CrossRef](#)]

**Disclaimer/Publisher’s Note:** The statements, opinions and data contained in all publications are solely those of the individual author(s) and contributor(s) and not of MDPI and/or the editor(s). MDPI and/or the editor(s) disclaim responsibility for any injury to people or property resulting from any ideas, methods, instructions or products referred to in the content.